



NIH Public Access

Author Manuscript

Histochem Cell Biol. Author manuscript; available in PMC 2010 January 1.

Published in final edited form as:

Histochem Cell Biol. 2009 January ; 131(1): 1–12. doi:10.1007/s00418-008-0505-9.

Spiny versus stubby: 3D reconstruction of human myenteric (type I) neurons

Tobias M. Lindig

Department of Anatomy I, University of Erlangen-Nuremberg, Krankenhausstraße 9, 91054 Erlangen, Germany

Section of Experimental Magnetic Resonance of the CNS, University of Tuebingen, 72076 Tuebingen, Germany

Surgical Planning Laboratory, Department of Radiology, Harvard Medical School, Brigham and Women's Hospital, Boston, MA 02115, USA

Vinod Kumar

Section of Experimental Magnetic Resonance of the CNS, University of Tuebingen, 72076 Tuebingen, Germany

Ron Kikinis

Surgical Planning Laboratory, Department of Radiology, Harvard Medical School, Brigham and Women's Hospital, Boston, MA 02115, USA

Steve Pieper

Surgical Planning Laboratory, Department of Radiology, Harvard Medical School, Brigham and Women's Hospital, Boston, MA 02115, USA

Isomics Inc., Cambridge, MA 02115, USA

Falk Schrödl, Winfried L. Neuhuber, and Axel Brehmer

Department of Anatomy I, University of Erlangen-Nuremberg, Krankenhausstraße 9, 91054 Erlangen, Germany

Abstract

We have compared the three-dimensional (3D) morphology of stubby and spiny neurons derived from the human small intestine. After immunohistochemical triple staining for leu-enkephalin (ENK), vasoactive intestinal peptide (VIP) and neurofilament (NF), neurons were selected and scanned based on their immunoreactivity, whether ENK (stubby) or VIP (spiny). For the 3D reconstruction, we focused on confocal data pre-processing with intensity drop correction, non-blind deconvolution, an additional compression procedure in z-direction, and optimizing segmentation reliability. 3D Slicer software enabled a semi-automated segmentation based on an objective threshold (interrater and intrarater reliability, both 0.99). We found that most dendrites of stubby neurons emerged only from the somal circumference, whereas in spiny neurons, they also emerged from the luminal somal surface. In most neurons, the nucleus was positioned abluminally in its soma. The volumes of spiny neurons were significantly larger than those of stubby neurons (total mean of stubbies $806 \pm 128 \mu\text{m}^3$, of spines $2,316 \pm 545 \mu\text{m}^3$), and spiny neurons had more dendrites (26.3 vs. 11.3). The ratios of somal versus dendritic volumes were 1:1.2 in spiny and 1:0.3 in stubby neurons. In conclusion, 3D reconstruction revealed new differences between stubby and spiny neurons and allowed estimations of volumetric data of these neuron populations.

Keywords

Neuron type; Confocal microscopy; Gut; Enteric nervous system; Innervation

Introduction

Neuronal intermediate filaments are important cytoskeletal structures that maintain neuronal shape and function and add rigidity, tensile strength and intracellular transport guidance within neuronal cell bodies and along dendritic and axonal processes (Julien 1999; Liu et al. 2004; Braissant 2007; Yuan 2007). Neurofilaments (NF) are type IV intermediate filaments composed of three subunits: light, medium and heavy protein chains. They are present in subpopulations of both central and peripheral neurons (Vickers and Costa 1992; Eaker 1997); other neuronal intermediate filaments are α -internexin and peripherin (Yuan 2007).

It has been a persistent challenge to characterize anatomical structures to provide a solid basis for any pathological assessment. The works of Ramón y Cajal (1911) were mainly based on a silver impregnation method, which established the foundation of modern neuroscience. Decades later, it was shown that the distribution pattern of silver staining in the central nervous system of the guinea pig correlates with that of NF immunostaining (Vickers and Costa 1992). Similarly, enteric neuron types described by silver impregnation (Stach 1989; Stach et al. 2000) were verified by NF immunohistochemistry in pig and human intestines (Brehmer 2006). Thus, NF immunohistochemistry provides the basis for combined morpho-chemical phenotyping of enteric neuron types.

Two of the human myenteric neuron types recently distinguished are the stubby and spiny (type I) neurons. Both resemble the original Dogiel type I neurons in that they have rather short dendrites and one axon (Dogiel 1899). Neurons with stubby-shaped dendrites and axons primarily running orally displayed immunoreactivity for enkephalin (ENK; Brehmer et al. 2005), whereas neurons with spiny shaped dendrites and axons running anally were co-immunoreactive for vasoactive intestinal peptide (VIP) and neuronal nitric oxide synthase (nNOS; Brehmer et al. 2006).

At first glance, the morphological differences between stubby and spiny neurons are not very distinct. Since they have not yet been directly compared and contrasted, this study has been undertaken to do so. We compared them morphometrically by measuring the classical parameters (somal area, dendritic field area) first, and then applied a three-dimensional (3D) reconstruction of their NF-immunostained cytoskeleton. For this purpose, we tried to find a way to reveal the most realistic, three-dimensional structure of NF-immunoreactive human myenteric neurons based on confocal serial sections, making a quantitative volumetric approach feasible. The method provided had to be compatible with normal, up-to-date hardware and possess a proven, highly reliable segmentation, and subsequent volume reconstruction, method regarding inter- and intrarater variability.

Next, we compared qualitatively and quantitatively 3D-reconstructed examples of both the neuron types. We suggest that the 3D visualization of neurons provides more realistic information about the morphology of their NF skeleton and about the quantitative differences between somata and dendrites of these two types than the usual two-dimensional depiction used in our earlier studies. To our knowledge, very few attempts were made to three-dimensionally reconstruct enteric neurons of laboratory animals on the basis of ultrathin or confocal serial sections; no attempts were made in humans (Ermilov et al. 2003; Hanani et al. 1998; Pompolo and Furness 1990; Szurszewski et al. 2002).

Materials and methods

Tissue processing

The use of human tissue for our experiments was approved by the Ethical Committee of the University of Erlangen-Nuremberg. The tissue samples originated from six human beings, and reconstructions were done from two gut segments from the body donor to the Institute of Anatomy (Table 1).

Segments of the five patients were transported in iced physiological saline to the laboratory. Segments of the body donor were from the duodenum (anal from the choledochoduodenal junction) and ileum (30 cm oral from the ileocaecal junction; post mortem time 4 h). All segments were rinsed within Kreb's solution at room temperature, and transferred into Dulbecco's modified Eagle's medium (DME/F12-Ham, Sigma Chemical Company, St Louis, MO, USA) containing 10 mg/ml antibiotic-antimycotic (Sigma), 50 µg/ml gentamycin (Sigma), 2.5 µg/ml amphotericin B (Sigma), 10% fetal bovine serum (Sigma), 4 µM nicardipine and 2.1 mg/ml NaHCO₃, bubbled with 95% O₂ and 5% CO₂ at 37°C for 1 h. Next, they were incubated for 5 h in the same medium with 100 µM colchicine, added to enhance peptide immunoreactivities in the neuronal somata.

For fixation, samples were pinned out on a Sylgard-lined Petri dish and transferred into 4% formalin in 0.1 M phosphate buffer (pH 7.4) at room temperature for 2 h. After several washes in 0.05 M tris-buffered saline (TBS; pH 7.4), two wholmounts derived from each segment (2 × 7 segments from six human beings) were prepared by scraping off the mucosa and removing the submucous and circular muscle layers. This resulted in longitudinal muscle/myenteric plexus wholmounts which were subjected to the following staining protocol.

Immunohistochemistry

Seven wholmount specimens (from each of the five patients and from the duodenum and ileum of the body donor) were preincubated for 2 h in 0.05 M TBS (pH 7.4), containing 1% bovine serum albumin (BSA), 0.5% Triton X-100, 0.05% thimerosal and 5% normal donkey serum. After a 10 min rinse in TBS, they were incubated in a solution containing BSA, Triton X-100, thimerosal (see above) and primary antibodies (leu-ENK, Biotrend/Germany: 4140-0204, raised in rabbit, dilution 1:200; VIP, Progen/Germany: 16071, guinea pig, 1:500; NF, Sigma/Missouri: 0142, mouse, 1:200) for 72 h (4°C). After an overnight rinse in TBS at 4°C, specimens were incubated in a solution equivalent to the first, but with secondary antibodies added, rather than primary antibodies (ALEXA Fluor 555 donkey anti-rabbit, MoBiTec/Germany: A-31572, 1:1.000; CyTM5 donkey anti-guinea pig, Dianova/Germany: 706-175-148, 1:100; ALEXA Fluor 488 donkey anti-mouse, MoBiTec/Germany: A-21202, 1:1.000; 4 h; room temperature), followed by an overnight rinse in TBS (4°C).

To reduce lipofuscin induced autofluorescence, wholmounts were incubated in ammonium acetate buffer (pH 5.0) containing 1 mM CuSO₄ for 60 min, followed by a short rinse in distilled H₂O (Schnell et al. 1999; Brehmer et al. 2004a).

Next, the wholmounts were mounted with TBS-glycerol (1:1; pH 8.6).

The remaining seven wholmounts were incubated in solutions lacking primary antisera. They were used as negative controls and showed no staining.

Quantification by area measurements

In each of the five wholmounts (of patients) triple-stained for ENK/VIP/NF, we randomly selected ten ENK-/NF-positive stubby neurons and ten VIP-/NF-positive spiny neurons in a

meander-like fashion. For this purpose, we used a digital camera system (Spot-RT-realtime, Visitron Systems, Munich, Germany) attached to a Leica Aristoplan microscope and SPOT advanced software (Version 3.5.6 for Windows, Diagnostic Instruments, USA). Of these 100 neurons, we measured their somal and dendritic field areas (by outlining the endings of all primary dendrites Brehmer et al. 2005; for statistical comparison see below).

Image acquisition and processing for 3D reconstruction

All together, 20 neurons were randomly selected in the two wholemounts. Ten neurons (five duodenal, five ileal), which displayed reactivity for VIP and NF but not for ENK, as well as ten neurons displaying co-reactivity for ENK and NF but not for VIP were scanned. For image acquisition, we used a Bio-Rad MRC 1000 confocal laser scanning microscope attached to a Nikon diaphot 300 equipped with a krypton–argon laser (American Laser Corporation, Salt Lake City, UT, USA). Z-series were created at three different excitation wave lengths. The filter settings were 568 nm excitation/filter 605 DF322 (ALEXA Fluor 555), 488 nm/522 DF32 (ALEXA Fluor 488) and 647 nm/680 DF322 (Cy5). A 40 \times oil immersion objective lens with a numerical aperture of 1.3 was used to collect the initial data sets of selected neurons, which were scanned at a resolution of 512 \times 768 pixels using 0.6 μ m intervals along the optical axis. Zoom factors varied between 1.5 and 2 depending on the different cell dimensions. Final 3D reconstructions were corrected for these differences and are identical in scale. Neuron portraits and figure plates were prepared using Amira 3.1, Confocal Assistant 4.02, ImageJ 1.33, IrfanView 3.97, Adobe Photoshop CS and 3D Slicer 2.6.

3D reconstruction and quantitative evaluation

Each data set was resized to a power of two [here 512 \times 512 pixels (2⁹), to improve image processing performance (ImageJ 1.33)] and deconvolved separately after axial intensity drop correction (z-drop) using the standard, non-blind deconvolution from the amiraDeconv package (TGS Inc.). The deblurred 3D volume was computed by an iterative (here 12 iterations) maximum-likelihood image restoration algorithm using a measured point spread function (PSF) obtained from a so-called bead measurement. Sub-resolution fluorescent micro spheres (Molecular Probes' PS-Speck green-fluorescent microsphere: P7220, 0.175 μ m in diameter; Fig. 1) were imaged under the same conditions as the specimen on top of the wholemount. In order to make the bead measurement robust and reliable, six of such bead measurements were spatially aligned and averaged (adapted from Brandt 2002). Generally, the optical point spread function smears the image along the optical axis about three times that in the x- and y-direction as shown by Turner et al. (1997,2000). Since deconvolution compensates for the microscope's PSF, a substantial spread effect is still noticeable. Inspection shows that a compression procedure (Fig. 1) of 3 to 1 in the z-direction almost eliminates the residual spread effect along the optical axis (adapted from Weaver et al. 2004). We performed this z-compression by decreasing the voxel depth by a factor of 3 once we applied an auto-adjustment of brightness and contrast to the whole volume, followed by a conversion of the image stack into single PGM files (ImageJ 1.33, IrfanView 3.97). The received 8 bit single optical sections consisting of 256 grey values and a near isotropic voxel size with an edge dimension ranging from 0.2 to 0.3 μ m (depending upon the magnification) were loaded into 3D Slicer software (Pieper et al. 2004) and processed further for quantitative volumetric analyses. In order to do this, we performed a user-guided semi-automated segmentation, tracing the outline of the cell using the thresholding module in Slicer, followed by a manual expert-driven evaluation and correction where needed. Crossing or adjacent structures of interfering neuropil had to be identified and manually separated using the information from upper and lower slices of the whole volume. The threshold was set at a level two standard deviations above the average background of the image stack, plus an additional factor of 30 grey values to take into account the remaining in plane spread effect (adapted from Gibbins et al. 2003). The average background was estimated in over ten areas in different slices next to the cell surface (ImageJ),

taking care for the absence of any staining in these areas. Based on the segmentation, the volume of the neuronal cytoskeleton was measured with the MeasureVol module for the entire neuron without axon and could be further divided into soma and dendrites. Dendrites were considered to be extensions from the soma of more than 1 μm in length. 3D-surface models were generated using the ModelMaker module within Slicer and were exported as VRML (Virtual Reality Modelling Language) files or high resolution TIF-files. The interrater and intrarater reliability of the segmentation was tested by repetitive volumetric analysis of 10 confocal data sets.

Statistical testing included the Pearson correlation coefficient for interrater and intrarater reliability, paired with Student's *t*-test for statistical significance. A *p* value of <0.05 was considered statistically significant.

All of the preprocessing and 3D-reconstruction steps were done on consumer-grade hardware (suggested minimum requirements: Pentium 4 with 1 GB RAM and 128 MB 3D graphic card).

Results

Immunohistochemistry and two-dimensional morphology of neurons

Neurons co-immunoreactive for ENK and NF displayed the morphology of stubby neurons (Fig. 2a; Brehmer et al. 2004a,b,2005). They were uniaxonal, had relatively small somata and short, stubby dendrites.

Neurons co-immunoreactive for VIP and NF had somewhat larger somata and their dendrites were of medium length and partly branched with spiny tips (Fig. 2b; Brehmer et al. 2004a,b, 2006). We found no neurons co-immunoreactive for all three markers.

Area measurements and subsequent statistical evaluation revealed that both somal and dendritic field areas of spiny neurons were larger than those of stubby neurons. The somal areas of stubby neurons ranged between 297 and 436 μm^2 , dendritic field areas were between 782 and 978 μm^2 . The somal areas of spiny neurons were between 439 and 801 μm^2 , and the dendritic field areas ranged between 1743 and 3128 μm^2 (Table 2).

Confocal 3D reconstruction

Resolution of structure, contrast and signal-to-noise ratio were improved (Fig. 3) by axial intensity drop correction and a non-blind deconvolution of the initial confocal series. Making an accurate quantitative volumetric approach feasible, the still-noticeable residual spread effect along the optical axis after deconvolution was further eliminated by a compression procedure in z-direction. To reveal the final three-dimensional structure, 3D Slicer software was used to perform a semi-automated segmentation, based on an objective threshold, with subsequent 3D reconstruction and volume measurements.

Validation of the semi-automated segmentation procedure established an interrater and intrarater reliability of both 0.99 for total cell volumes (Pearson correlation coefficient '*r*').

Optimized preprocessing of inherent confocal aberrations, together with high segmentation reliability, led to a more realistic three-dimensional morphology of the NF cytoskeleton, providing significant new differences between stubby and spiny neurons.

Neuronal 3D morphology

Portraits of the luminal surfaces of the neurons reconstructed in this study were depicted in Figs. 4 (stubby neurons) and 5 (spiny neurons). Within the somata of stubby neurons, the NF immunoreactivity was observed to be distributed homogeneously. In contrast, in the somata of spiny neurons, the distribution pattern of NF immunoreactivity was inhomogeneous and its

intensity weaker (Fig. 6a). In most of the 20 neurons (9 spiny, 7 stubby), the nucleus was positioned eccentrically, near the abluminal surface of the soma (Fig. 6b). Only one stubby neuron displayed a more luminal position of its nucleus; in two stubby and one spiny neuron, the nucleus was in a central position.

All of the reconstructed neurons were Xattened in the plane of the myenteric plexus (thickness between 2 and 4 μm ; Table 3). Most of the dendrites emerged from the circumference of the somata and extended into this 'myenteric' plane. In addition, all 10 spiny neurons displayed dendrites emerging from the luminal somal surface (Figs. 5, 7). Spiny neurons with numerous 'luminal' dendrites displayed a hedgehog-like appearance, and two of them had additional abluminal short processes. Most stubby neurons exclusively displayed dendrites which emerged circumferentially, and only two of them had short dendrites on their luminal surface.

The axons of the 20 neurons investigated displayed a circular cross-sectional profile. In contrast, most dendrites' were oval shaped. Some of the spiny neurons had short extensions from their initial axonal segment (Fig. 5a, d, i, k).

Quantitative estimations, summarized in Table 3, showed that the total somal and dendritic volumes of spiny neurons were significantly larger than those of stubby neurons. This was also true for the somal and dendritic volumes when compared separately. The ratio of somal versus dendritic volume was about 1:1.2 in spiny neurons and about 1:0.3 in stubby neurons.

Discussion

This study has shown, via direct comparison, that stubby and spiny (type I) neurons differ morphologically, chemically and, hence, functionally. The population of 'Dogiel type I neurons' in the human myenteric plexus is heterogeneous and consists of at least two quite different neuron types. Stubby neurons may represent ascending inter- or motor neurons, and spiny neurons may be descending inter- or motor neurons (Brehmer 2006).

Methodological considerations

Most morphological studies of peripheral and central neurons are still based on two-dimensional imaging. However, several dye-filling studies in the peripheral nervous system (Ermilov et al. 2000, 2003, 2004; Miller et al. 1996; Hanani et al. 1998; Watkins and Keast 1999; Anderson et al. 2001, 2003; Rich et al. 2002; Szurszewski et al. 2002; Jobling et al. 2003) have used confocal microscopy for 3D reconstruction and volumetric quantification. Only one study in the pelvic ganglia of female guinea pigs (Jobling et al. 2003) used an auto-deconvolution step for data pre-processing to reject interfering out-of-focus information. As shown in Figs. 1 and 3, morphological measurements are likely to be inaccurate without reasonable correction of the microscope's point spread function, leading to an overestimation of quantitative measurements, particularly regarding volumetric approaches. Inspired by these earlier works, we tried to get one step ahead to a more realistic 3D structure of NF immunoreactive neurons. Therefore, emphasis was not only put on confocal data preprocessing, but also on optimizing segmentation reliability.

To foster our goal of making this method widely available, we mainly used open source software, except for the deconvolution step, in which the quality is still much better in commercial products. By keeping a close look on the computational burden, all steps presented in this work can be done on normal consumer-grade hardware or even on an up-to-date notebook. The outstanding visualization capabilities of 3D Slicer software, initially developed for MRI and CT data, were used to process optical-sectioning microscopy volume data. 3D Slicer is a medical visualization and processing environment for research and a platform for exploring novel image analysis and visualization techniques. An open source software

supported by the NA-MIC Community (National Alliance for Medical Image Computing), is freely available under <http://www.na-mic.org/Slicer/Download/>.

In confocal microscopy, convolution with distortion, in the form of an elongation mainly along the optical axis, due to refractive index mismatch among the tissue, mounting medium and optical pathway, turns points of light into so-called Airy disks. Since the intrinsic limitations of all confocal light microscope systems are especially apparent when thick sections like wholermounts are imaged (Holmes et al. 1995), good deconvolution has to be done to correct the microscope's z-axis distortion. To account for this, in our data pre-processing pipeline, we used an iterative non-blind deconvolution algorithm of the amiraDeconv package, followed by an additional compression step to further reduce the residual spread effect along the optical axis. In contrast to former works, we did not use a compression by voxel averaging since this may cause some loss of information. Maintaining the original amount of optical slices, we accomplished the compression in z-direction by decreasing the voxel depth instead.

To reduce errors arising from the subjectivity, inconsistency and fatigue that are unfortunately associated with a sole expert-driven manual segmentation, in our semi-automated workflow we implemented a thresholding procedure, based on the average background of each individual image stack, as a form of automatic tracing. The average background was measured in over ten areas in different slices with no obvious signal from any labeled structure next to the cell surface. Semiautomatic approaches combine the efficiency and repeatability of automatic segmentation with the sound judgement only human expertise can offer (Yushkevich et al. 2006). Since segmentation of anatomical structures in neuroimaging research is a fundamental task, literature shows inter- and intrarater reliabilities for semiautomated segmentations in the central nervous system of 0.91–0.99 (Klockgether et al. 1998; Luft et al. 1998, 1999; Okugawa et al. 2003).

In this study, the tissue was stretched before and during fixation which may have contributed to a more Xattened appearance of the neuronal somata (Gabella 1990). Flat-shaped peripheral neurons were also found in unstretched preparations by Miller et al. (1996), in mouse superior mesenteric ganglion. As shown in previous studies, peripheral autonomic neurons did not show any significant differences before fixation, after fixation, or after coverslipping (Hanani et al. 1998; Ermilov et al. 2000; Anderson et al. 2001). Significant decrease in volume and shape were reported only after dehydration procedures by Hanani et al. (1998), which were not used in this study.

To the authors' knowledge, this is the first study using NF staining for 3D reconstruction and volume evaluation in peripheral neurons. To search for a viable neuropathologic screening routine, one should stain as many neurons as possible and look for histopathological changes of single cells and for changes within the ganglion or plexus itself. Thus, dye-filling of single neurons does not seem to be an appropriate method for diagnostic evaluation. A more feasible approach may be the NF staining of enteric wholermounts where many ganglia are displayed at the same time, and show at least half of the whole enteric neuron population (Ganns et al. 2006). Since it is widely accepted that accumulation of NF (Brandt 2001; Liu et al. 2004) in neurodegenerative disorders are the hallmark of neuronal dysfunction, the precise three-dimensional visualization of the fine neuronal cytoskeleton anatomy may lead to a better understanding of the underlying pathology.

3D-reconstructed stubby and spiny neurons

This study showed that spiny neurons are larger than stubby neurons and, additionally, revealed some structural features of stubby and spiny neurons that could only be distinctly revealed after 3D reconstruction. In most neurons investigated, these are: the abluminal position of the

nucleus; the absence of luminal and abluminal dendrites in the majority of stubby neurons; and the presence of luminal, but absence of abluminal, dendrites in most spiny neurons.

The majority of dendrites in stubby and spiny (and, likely, of other) neurons emerge at the somal circumference. This may be a result of the location of myenteric neurons between two muscle layers and their Xattened appearance. In the case of an 'occupied' circumference (mainly in spiny neurons displaying more dendrites than stubby neurons), additional dendrites may appear on the luminal side of the soma, rather than on the abluminal. We do not currently have an explanation for this difference.

Pretreatment of colchicine may have influenced the shapes of the neurons and may have changed the sizes of stubby and spiny neurons differently. However, as we pointed out earlier, we have not yet observed morphological differences between neurons in material with and without colchicine-pretreatment (Brehmer et al. 2004b). Of course, this should be addressed in future studies.

For the first time, we have shown that there are substantial quantitative differences between the NF cytoskeletons of stubby and spiny neurons, via the direct comparison of neurons derived from the same wholemount. In the human small intestine, stubby neurons are smaller than spiny neurons. This has been shown both by conventional, two-dimensional measurements of somata and dendritic fields as well as by volumetric comparisons between the two neuron types. This is in line with the results of two previous studies where somal areas of stubby and of spiny neurons were compared with those of type II neurons, which are morphologically quite different. Stubby neurons were two to three times smaller than type II neurons (Brehmer et al. 2005), whereas there was only a slight difference between spiny and type II neurons (Brehmer et al. 2006).

Compared to the volumes of 3D-reconstructed enteric and peripheral neurons derived from laboratory animals (Hanani et al. 1998; Ermilov et al. 2000, 2003; Jobling et al. 2003), the values of the human myenteric neurons in this study are considerably smaller. This may be due to the different labeling of the neurons. All other authors filled the neurons with dye, i.e., the whole membrane-covered volume was reconstructed. In our study, 'only' NF (which does not occupy the whole cytoplasmatic compartment) has been marked as the basis for reconstruction.

A logical extension of our previous studies (Brehmer et al. 2004a, b, 2005, 2006), 3D reconstruction of the NF-labeled cytoskeleton revealed significant differences between the NF-stained cytoskeleton of stubby and spiny neurons—in other words, in the positions of dendritic origins and of nuclei within their somata. Furthermore, it allowed estimations of volumetric data of the two human myenteric neuron populations.

In conclusion, the results of this 3D-reconstruction study corroborate our concept of the differentiation of human type I neurons into stubby and spiny neurons displaying correlated differences in both chemistry and morphology.

Acknowledgments

The excellent technical assistance of Karin Löschner, Stephanie Link, Andrea Hilpert, Hedwig Symowski and Inge Zimmermann (all Erlangen) is gratefully acknowledged. We thank the Department of Molecular Plant Physiology (Erlangen) for helping with the deconvolution. We thank Mark Anderson (Boston), Ian Gibbins (Adelaide) and Christian Lauterbach (Erlangen) for their advice and feedback and Katie Mastrogiacomo (Boston) for carefully reading the manuscript. The study was supported by Deutsche Forschungsgemeinschaft (BR 1815/3) and National Institutes of Health (P41 RR13218 and U54 EB005149).

References

Anderson RL, Jobling P, Gibbins IL. Development of electrophysiological and morphological diversity in autonomic neurons. *J Neurophysiol* 2001;86:1237–1251. [PubMed: 11535673]

Anderson JR, Wilcox MJ, Wade PR, Barrett SF. Segmentation and 3D reconstruction of biological cells from serial slice images. *Biomed Sci Instrum* 2003;39:117–122. [PubMed: 12724879]

Braissant, O. Neurofilament proteins in brain diseases. In: Arlen, RK., editor. *New research on neurofilament proteins*. Nova Science Publishers; New York: 2007. p. 25-51.

Brandt R. Cytoskeletal mechanisms of neuronal degeneration. *Cell Tissue Res* 2001;305:255–265. [PubMed: 11545263]

Brandt, R. Increasing image fidelity with amiraDECONV™. Amira 3.0. 2002. www.amiravis.com

Brehmer A. Structure of enteric neurons. *Adv Anat Embryol Cell Biol* 2006;186:1–94. [PubMed: 16909915]

Brehmer A, Blaser B, Seitz G, Schrödl F, Neuhuber W. Pattern of lipofuscin pigmentation in nitrenergic and non-nitrenergic, neurofilament immunoreactive myenteric neuron types of human small intestine. *Histochem Cell Biol* 2004a;121:13–20. [PubMed: 14663589]

Brehmer A, Croner R, Dimmler A, Papadopoulos T, Schrödl F, Neuhuber W. Immunohistochemical characterization of putative primary afferent (sensory) myenteric neurons in human small intestine. *Auton Neurosci* 2004b;112:49–59. [PubMed: 15233930]

Brehmer A, Lindig TM, Schrödl F, Neuhuber W, Ditterich D, Rexer M, Rupprecht H. Morphology of enkephalin-immunoreactive myenteric neurons in the human gut. *Histochem Cell Biol* 2005;123:131–138. [PubMed: 15776249]

Brehmer A, Schrödl F, Neuhuber W. Morphology of VIP/nNOS-immunoreactive myenteric neurons in the human gut. *Histochem Cell Biol* 2006;125:557–565. [PubMed: 16328433]

Dogiel AS. Ueber den Bau der Ganglien in den Geflechten des Darmes und der Gallenblase des Menschen und der Säugethiere. *Arch Anat Physiol Anat Abt (Leipzig)* 1899;130–158.

Eaker EY. Neurofilament and intermediate filament immunoreactivity in human intestinal myenteric neurons. *Dig Dis Sci* 1997;42:1926–1932. [PubMed: 9331157]

Ermilov LG, Miller SM, Schmalz PF, Hanani M, Szurszewski JH. The three-dimensional structure of neurons in the guinea pig inferior mesenteric and pelvic hypogastric ganglia. *Auton Neurosci* 2000;83:116–126. [PubMed: 11593762]

Ermilov LG, Miller SM, Schmalz PF, Hanani M, Lennon VA, Szurszewski JH. Morphological characteristics and immunohistochemical detection of nicotinic acetylcholine receptors on intestinofugal afferent neurones in guinea-pig colon. *Neurogastroenterol Motil* 2003;15:289–298. [PubMed: 12787338]

Ermilov LG, Schmalz PF, Miller SM, Szurszewski JH. PACAP modulation of the colon-inferior mesenteric ganglion reflex in the guinea pig. *J Physiol* 2004;560:231–247. [PubMed: 15284351]

Gabella G. On the plasticity of form and structure of enteric ganglia. *J Auton Nerv Syst* 1990;30:S59–S66. [PubMed: 2212494]

Ganns D, Schrödl F, Neuhuber W, Brehmer A. Investigation of general and cytoskeletal markers to estimate numbers and proportions of neurons in the human intestine. *Histol Histopathol* 2006;21:41–51. [PubMed: 16267786]

Gibbins IL, Teo EH, Jobling P, Morris JL. Synaptic density, convergence, and dendritic complexity of prevertebral sympathetic neurons. *J Comp Neurol* 2003;455:285–298. [PubMed: 12483682]

Hanani M, Ermilov LG, Schmalz PF, Louzon V, Miller SM, Szurszewski JH. The three-dimensional structure of myenteric neurons in the guinea-pig ileum. *J Auton Nerv Syst* 1998;71:1–9. [PubMed: 9722188]

Holmes, TJ.; Bhattacharyya, S.; Cooper, JA.; Hanzel, D.; Krishnamurthi, V.; Lin, W.; Roysam, B.; Szarowski, DH.; Turner, JN. Light microscopic images reconstructed by maximum likelihood deconvolution. In: Pawley, JB., editor. *Handbook of biological confocal microscopy*. Plenum; New York: 1995. p. 389-402.

Jobling P, Gibbins IL, Morris JL. Functional organization of vasodilator neurons in pelvic ganglia of female guinea pigs: comparison with uterine motor neurons. *J Comp Neurol* 2003;459:223–241. [PubMed: 12655506]

Julien JP. Neurofilament functions in health and disease. *Curr Opin Neurobiol* 1999;9:554–560. [PubMed: 10508735]

Klockgether T, Skalej M, Wedekind D, Luft AR, Welte D, Schulz JB, Abele M, Burk K, Laccone F, Brice A, Dichgans J. Autosomal dominant cerebellar ataxia type I. MRI-based volumetry of posterior fossa structures and basal ganglia in spinocerebellar ataxia types 1, 2 and 3. *Brain* 1998;121:1687–1693. [PubMed: 9762957]

Liu Q, Xie F, Siedlak SL, Nunomura A, Honda K, Moreira PI, Zhua X, Smith MA, Perry G. Neurofilament proteins in neurodegenerative diseases. *Cell Mol Life Sci* 2004;61:3057–3075. [PubMed: 15583867]

Luft AR, Skalej M, Welte D, Kolb R, Burk K, Schulz JB, Klockgether T, Voigt K. A new semiautomated, three-dimensional technique allowing precise quantification of total and regional cerebellar volume using MRI. *Magn Reson Med* 1998;40:143–151. [PubMed: 9660564]

Luft AR, Skalej M, Schulz JB, Welte D, Kolb R, Burk K, Klockgether T, Voigt K. Patterns of age-related shrinkage in cerebellum and brainstem observed in vivo using three-dimensional MRI volumetry. *Cereb Cortex* 1999;9:712–721. [PubMed: 10554994]

Miller SM, Hanani M, Kuntz SM, Schmalz PF, Szurszewski JH. Light, electron, and confocal microscopic study of the mouse superior mesenteric ganglion. *J Comp Neurol* 1996;365:427–444. [PubMed: 8822180]

Okugawa G, Takase K, Nobuhara K, Yoshida T, Minami T, Tamagaki C, Magnotta VA, Andreasen NC, Kinoshita T. Inter- and intraoperator reliability of brain tissue measures using magnetic resonance imaging. *Eur Arch Psychiatry Clin Neurosci* 2003;253:301–306. [PubMed: 14714119]

Pieper, S.; Halle, M.; Kikinis, R. 3D slicer; Proceedings of IEEE international symposium on biomedical imaging: from nano to macro 2004; 2004. p. 632-635. SPL technical report #448

Pompolo S, Furness JB. Ultrastructure and synaptology of neurons immunoreactive for gamma-aminobutyric acid in the myenteric plexus of the guinea pig small intestine. *J Neurocytol* 1990;19:539–549. [PubMed: 2243246]

Ramón, y; Cajal, S. *Histologie du système nerveux de l'homme et des vertébrés*. Maloine; Paris: 1911.

Rich A, Hanani M, Ermilov LG, Malysz J, Belzer V, Szurszewski JH, Farrugia G. Physiological study of interstitial cells of Cajal identified by vital staining. *Neurogastroenterol Motil* 2002;14:189–196. [PubMed: 11975719]

Schnell SA, Staines WA, Wessendorf MW. Reduction of lipofuscin-like autofluorescence in fluorescently labeled tissue. *J Histochem Cytochem* 1999;47:719–730. [PubMed: 10330448]

Stach, W. A revised morphological classification of neurons in the enteric nervous system. In: Singer, MV.; Goebell, H., editors. *Nerves and the gastrointestinal tract*. Kluwer; Lancaster: 1989. p. 29-45.

Stach, W.; Krammer, H-J.; Brehmer, A. Structural organization of enteric nerve cells in large mammals including man. In: Krammer, H-J.; Singer, MV., editors. *Neurogastroenterology from the basics to the clinics*. Kluwer; Dordrecht: 2000. p. 3-20.

Szurszewski JH, Ermilov LG, Miller SM. Prevertebral ganglia and intestinofugal afferent neurones. *Gut* 2002;51(suppl 1):i6–i10. [PubMed: 12077055]

Turner JN, Ancin H, Becker DE, Szarowski DH, Holmes M, O'Connor N, Wang M, Holmes T, Roysam B. Automated image analysis technologies for biological 3D light microscopy. *Int J Imag Syst Tech* 1997;8:240–254.

Turner JN, Shain W, Szarowski DH, Lasek S, Dowell N, Sipple B, Can A, Al-Kofahi K, Roysam B. Three-dimensional light microscopy: observation of thick objects. *J Histotechnol* 2000;23:205–217.

Vickers JC, Costa M. The neurofilament triplet is present in distinct subpopulations of neurons in the central nervous system of the guinea-pig. *Neuroscience* 1992;49:73–100. [PubMed: 1407552]

Watkins TW, Keast JR. Androgen-sensitive preganglionic neurons innervate the male rat pelvic ganglion. *Neuroscience* 1999;93:1147–1157. [PubMed: 10473279]

Weaver CM, Hof FR, Wearne SL, Lindquist WB. Automated algorithms for multiscale morphometry of neuronal dendrites. *Neural Comput* 2004;16:1353–1383. [PubMed: 15165394]

Yuan, A. Neurofilament protein partnership, export, transport, phosphorylation and neurodegeneration. In: Arlen, RK., editor. *New research on neurofilament proteins*. Nova Science Publishers; New York: 2007. p. 53-79.

Yushkevich PA, Piven J, Hazlett HC, Smith RG, Ho S, Gee JC, Gerig G. User-guided 3D active contour segmentation of anatomical structures: significantly improved efficiency and reliability. *Neuroimage* 2006;31:1116–1128. [PubMed: 16545965]

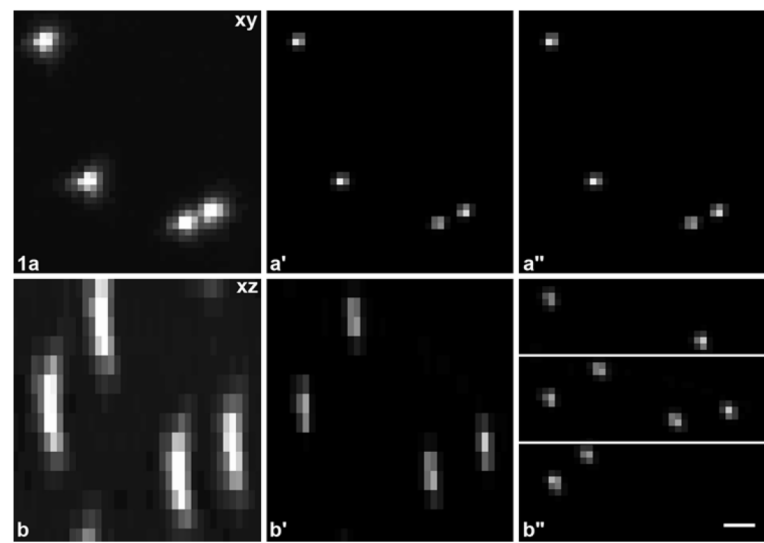


Fig. 1.

Confocal maximum value projections of single sub-resolution spheres (Molecular Probes' PS-Speck green-fluorescent microspheres) in *xy* (a) and *xz* (b) view, *upper and lower row* (a, b) raw data; (a', b') deconvolved data; (a'', b'') after deconvolution with z-compression of 3 to 1. The distance between the two *white lines* in b'' corresponds to the total height of b and b' after compression by a factor of 3 along the optical axis. Voxel size $0.2 \times 0.2 \times 0.6 \mu\text{m}$ (a, a'; b, b') and $0.2 \times 0.2 \times 0.2 \mu\text{m}$ (a'', b''). *Scale bar* 1 μm

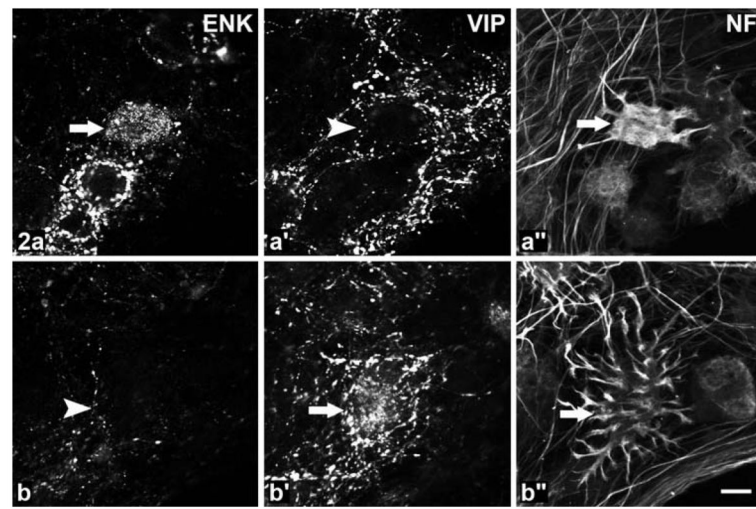
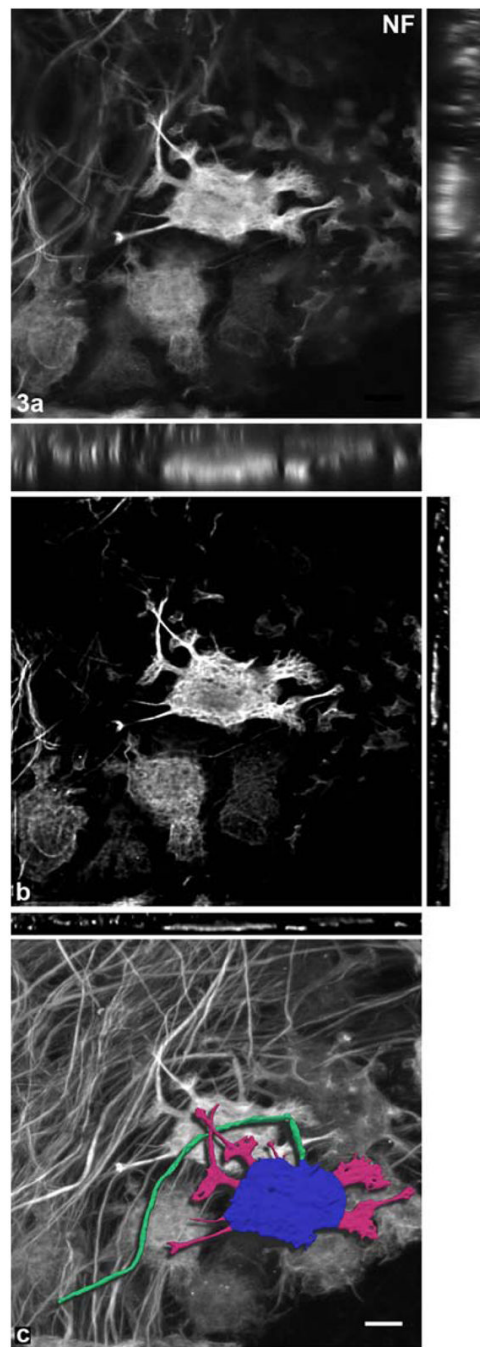
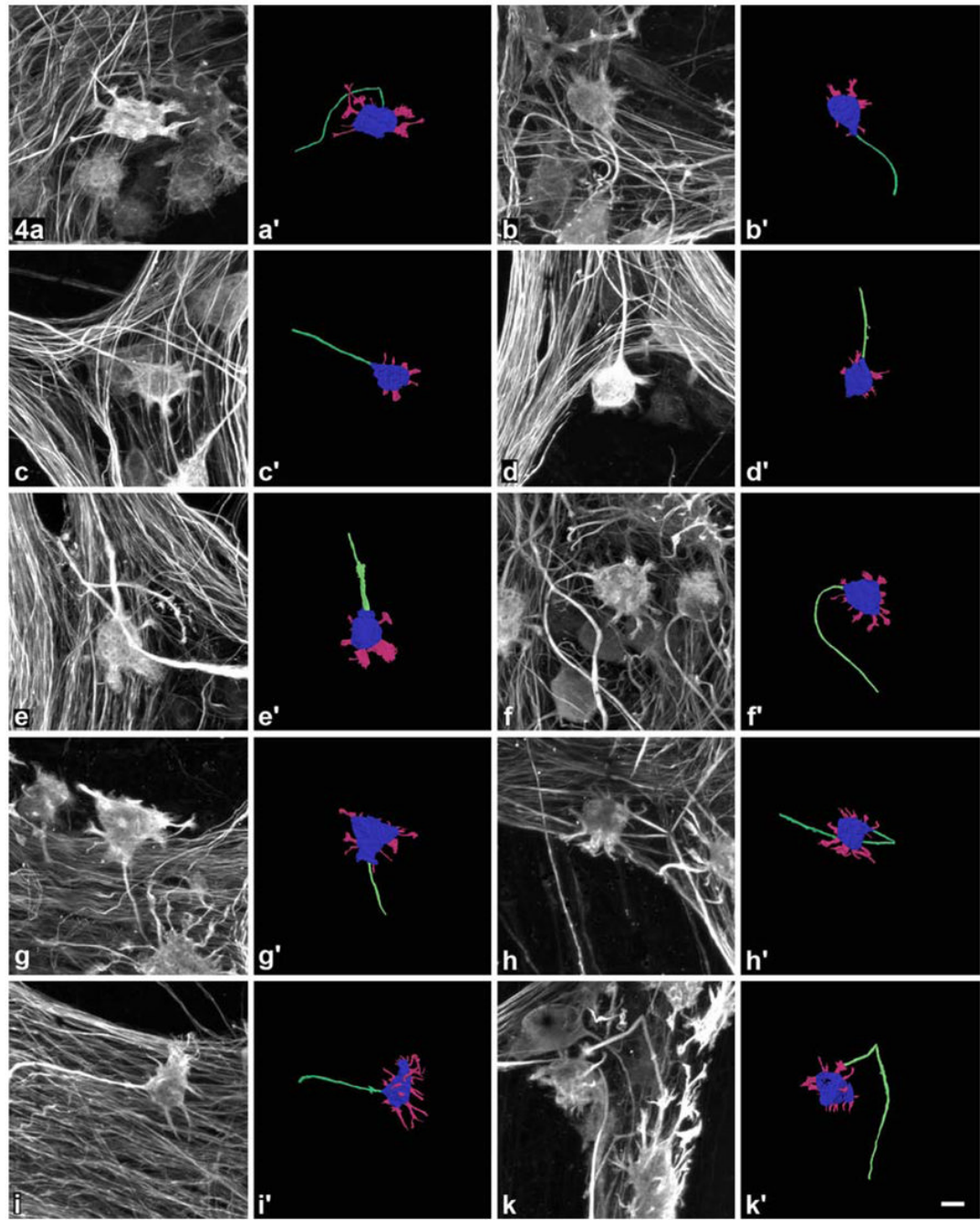


Fig. 2.

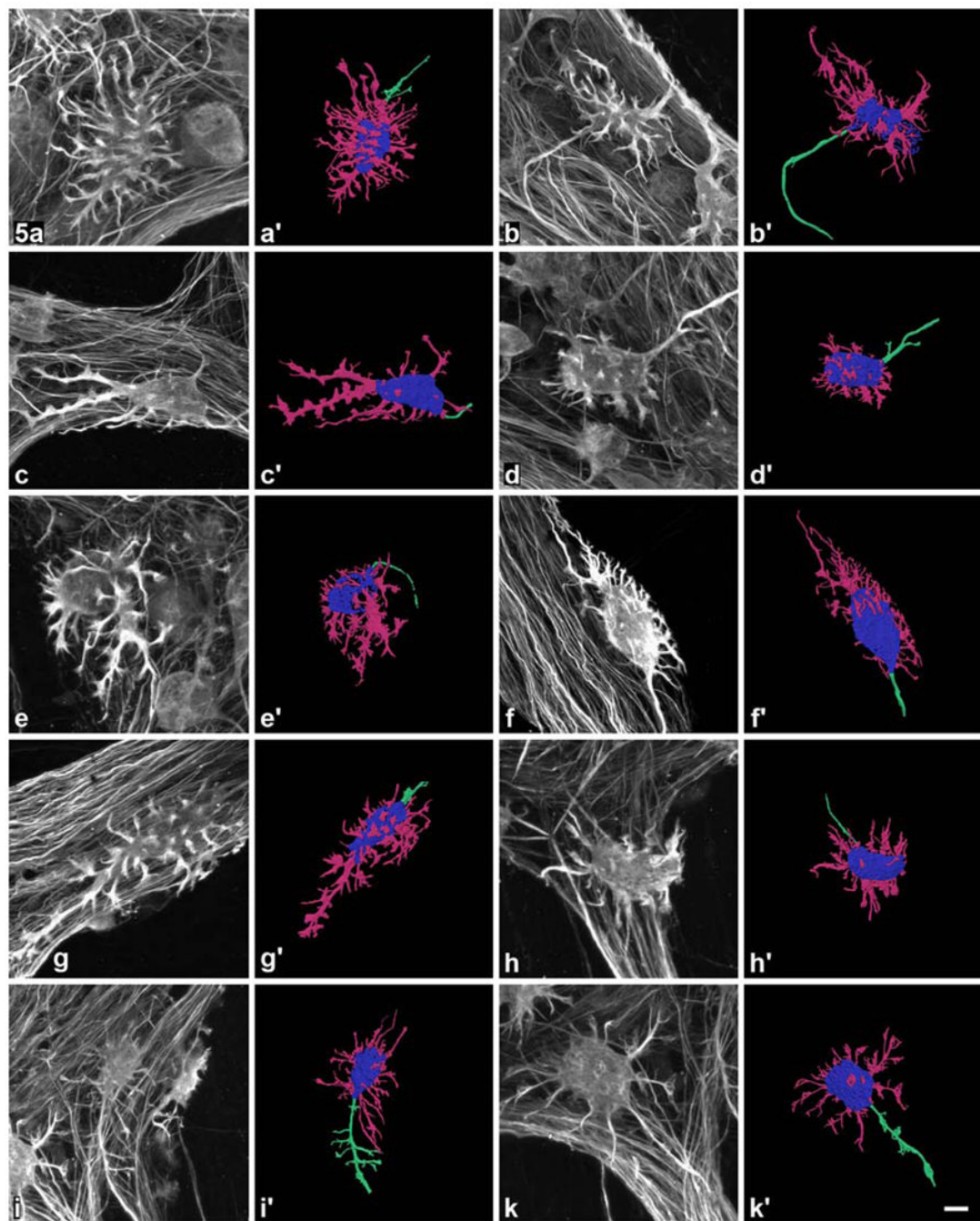
Different morphologies of leu-enkephalin (ENK)- and of vasoactive intestinal peptide (VIP)-immunoreactive neurons. (a) A neuron immunoreactive for ENK (arrow), negative for VIP (a'; arrowhead) and coimmunoreactive for neurofilament (NF) (a''; arrow) is morphologically a stubby neuron. (b) Another neuron is negative for ENK (a; arrowhead) but positive for both VIP (b'; arrow) and NF (b''; arrow), this is a spiny neuron. Scale bar 10 μ m

**Fig. 3.**

Single confocal section image of the same stubby neuron shown in Fig. 2: before (a) and after (b) preprocessing, including: z-drop correction, non-blind deconvolution, brightness/contrast adjustment and z-compression; single slice orthogonal view. In c the colored 3D-reconstructed neurofilament cytoskeleton (NF; soma blue, dendrites red, axon green) is displayed on the original raw data. *Scale bar* 10 μ m

**Fig. 4.**

Ten neurofilament (NF)-stained stubby neurons [five from duodenum (a–e), five from ileum (f–k)] are depicted twice in luminal view: in the extended focus mode (*left picture*) and after 3D reconstruction (*right picture*; soma blue, dendrites red, axon green). The latter are shown in 15° rotation out of the confocal plane. The neuron in (a) is the same neuron as in Figs. 2 and 3. Also all other neurons were positive for leu-enkephalin but negative for vasoactive intestinal peptide (not shown). *Scale bar* 10 μm

**Fig. 5.**

Ten neurofilament (NF)-stained spiny neurons [five from duodenum (a–e), five from ileum (f–k)] are depicted twice in luminal view: in the extended focus mode (*left picture*) and after 3D reconstruction (*right picture*; soma blue, dendrites red, axon green). The latter are shown in 15° rotation out of the confocal plane. The neuron in (a) is the same neuron as in Fig. 2. All other neurons were positive for vasoactive intestinal peptide but negative for leu-enkephalin (not shown). *Scale bar* 10 μm

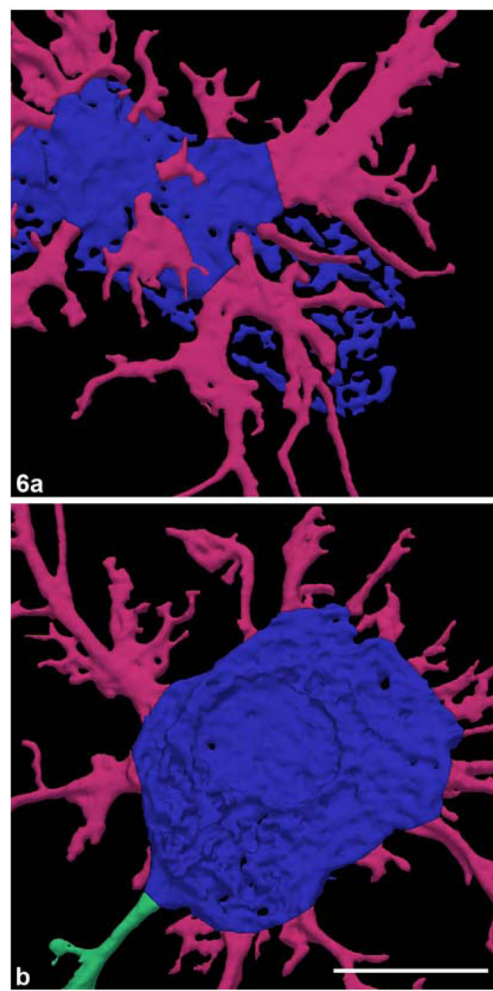


Fig. 6.
a The somal region of the spiny neuron in Fig. 5b is enlarged, the neurofilament-distribution (blue) within the soma is inhomogeneous. **b** The spiny neuron from Fig. 5k is enlarged and seen in abluminal view, and the position of the nucleus is seen as a trough. *Scale bar* 10 μ m

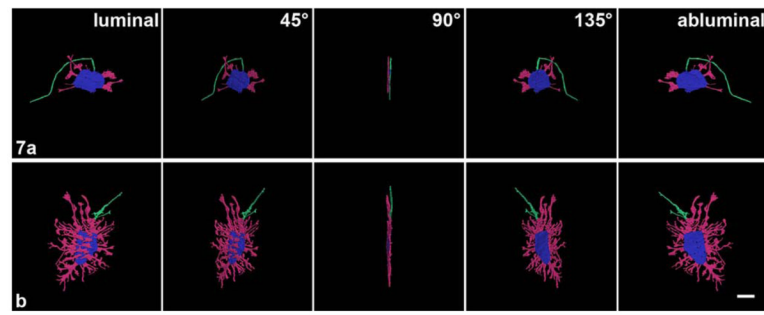


Fig. 7.

Two neurons are rotated in four steps (45° – 180°) from luminal to the abluminal view (soma *blue*, dendrites *red*, axon *green*). The stubby neuron (**a**) has only dendrites emerging from the circumference. The spiny neuron (**b**) displays additional dendrites emerging from the luminal but not from the abluminal somal surface. *Scale bar* 10 μm

Data of human gut segments used

Table 1

Segment	Age	Sex	Disease
Duodenum	28	Male	Pancreas carcinoma
Duodenum	42	Female	Pancreas carcinoma
Duodenum/jejunum	67	Male	Pancreas carcinoma
Ileum	57	Female	Caecum carcinoma
Ileum	58	Male	Colon carcinoma
Duodenum + ileum	75	Male	Cardiopulmonary failure (donor)

The first five human beings were patients undergoing surgery for carcinoma, the last one was a body donor to the Institute of Anatomy who did not suffer from gastrointestinal disease

Table 2

Somal areas and dendritic field areas of each ten stubby and spiny neurons (mean values \pm standard deviations; μm^2) derived from the five patients who suffered from carcinoma

	Stubby neurons		Spiny neurons	
	Somal area	Dendritic area	Somal area	Dendritic area
28 Duodenum	436 \pm 96.8	978 \pm 213	801 \pm 151	3128 \pm 505.4
42 Duodenum	335 \pm 127.7	811 \pm 242.5	636 \pm 48.8	3112 \pm 842.1
67 Duodenum	323 \pm 67.1	782 \pm 180.6	619 \pm 79	2903 \pm 574.1
57 Ileum	323 \pm 54.4	800 \pm 163.5	439 \pm 76.1	1743 \pm 468.7
58 Ileum	297 \pm 84.9	850 \pm 223.7	524 \pm 111.2	2742 \pm 844.6

Statistical comparison revealed that all somal areas of stubby neurons were smaller than those of spiny neurons of the same patient, the same referred to dendritic field areas of stubby versus those of spiny neurons (all p values < 0.01)

Table 3Mean values (\pm standard deviations) of ten stubby (depicted in Fig. 4) and ten spiny neurons (depicted in Fig. 5)

	Somal length	Somal width	Somal thickness	Total volume	Somal volume	Dendritic volume	Dendritic number
Stubby/duodenum	27.7 \pm 1.4	19.8 \pm 1.5	3 \pm 0.5	777.4 \pm 114.6	591 \pm 40.5	186.4 \pm 107.6	8 \pm 1.9
Stubby/ileum	28.9 \pm 3.8	22.1 \pm 4.6	3.3 \pm 1	834.4 \pm 160.5	612.6 \pm 117.5	222 \pm 91.2	14.6 \pm 3.6
Stubby/total	28.3 \pm 2.7	21.0 \pm 3.3	3.1 \pm 0.7	806 \pm 128	602 \pm 79	204 \pm 91	11.3 \pm 4.2
p-values	<0.01			<0.01	<0.01	<0.01	<0.01
Spiny/total	42.5 \pm 7.6	22.8 \pm 3.3	3.2 \pm 0.7	2,316 \pm 545	1,070 \pm 424	1,246 \pm 452	264 \pm 57
Spiny/duodenum	41.4 \pm 6.5	23.1 \pm 3.2	2.9 \pm 0.5	2,215.8 \pm 643.6	866.4 \pm 401.3	1,349.4 \pm 549.7	22.6 \pm 4.8
Spiny/ileum	43.5 \pm 9.9	22.6 \pm 4.0	3.4 \pm 0.9	2,415.2 \pm 551.7	1,273.2 \pm 430.3	1,142 \pm 425.6	30.2 \pm 4.5

Linear values in μm , volumes in μm^3

The first five each derived from the duodenum, the others from the ileum of the body donor (75 years, male)

P values refer to statistical comparisons between total values of stubby with those of spiny neurons